Materials Science in Semiconductor Processing 16 (2013) 274–281

Contents lists available at SciVerse ScienceDirect

Materials Science in Semiconductor Processing

journal homepage: www.elsevier.com/locate/mssp

Nanostructured metal–insulator–metal capacitor with anodic titania

D. Kannadassan [a], R. Karthik [a], Maryam Shojaei Baghini [b], P.S. Mallick [a,*]

[a] VIT University, Vellore – 632014, Tamilnadu, India
[b] Department of Electrical Engineering, Indian Institute of Technology – Bombay, Mumbai-76, India

ARTICLE INFO

Available online 14 December 2012

Keywords:
Anodization
Dielectric polarization
Frequency dependent capacitance
Leakage mechanisms
Crystalline properties

ABSTRACT

This paper presents fabrication and electrical characterization of barrier type TiO_2 metal–insulator–metal (MIM) capacitor using anodization. Polarization process, conduction mechanisms, and structural properties are studied in detail. We found that the anodization voltage played a major role in electrical and structural properties of the thin film. The barrier type anodic TiO_2 is suggested as a dielectric material for high-performance MIM capacitors.

1. Introduction

High-capacitance density, reduced leakage, and enhanced reliability are the major challenges for metal–insulator–metal (MIM) capacitors. According to ITRS 2010 [1], MIM capacitors should hold a capacitance density of 10 fF/μm^2, leakage current density $< 1 \times 10^{-8}$ A/cm^2, and quadratic voltage coefficient of the capacitance (VCC) $\alpha < 100$ ppm/V^2 by 2018. Capacitance density can be improved by reducing the thickness of the dielectric layer, which is limited by fabrication methods and reliability issues. Many high-k dielectric materials such as HfO_2, ZrO_2, Al_2O_3, and TiO_2 are used to meet the challenges [2–5].

Titanium oxide or titania (TiO_2) is an attractive material that has evolved with considerable interest in a variety of applications such as gas sensors, photovoltaic devices, and capacitors [6–8]. TiO_2 naturally exists in three crystalline phases, namely rutile, anatase, and brookite, with a dielectric constant of 40–170 and energy bandgap of ~3.0 eV [9]. Recently, TiO_2 MIM capacitors have been fabricated using thermal oxidation [8] and DC magnetron sputtering [10]. Thermal oxidation and DC magnetron sputtering yield MIM capacitors with high leakage current density ($> 10^{-4}$ A/cm^2) and capacitance variation $\Delta C/C_0 > 10^4$ ppm [8,10]. This is due to the structural defects/traps available in bulk oxide and near to metal/insulator interface.

Anodization is an attractive preparation method of high-k metal oxide thin films with low defect and improved polarization, which has been investigated by many authors [11–14]. During anodization, the barrier type oxide is formed if the resultant anodic oxide is insoluble in the electrolyte [15]. However, if resulting anodic oxide is soluble in electrolyte, it produces porous anodic structures. We have already fabricated MIM capacitors using barrier-type anodic alumina and studied the electrical properties in detail [11]. Using an electrode polarization model, it has been found that the low defect density and improved ionic polarization result in a low VCC of 500 ppm/V and low leakage current density of 1 nA/cm^2 at 2 V [11]. However, to the best of our knowledge, no report is available on fabrication and electrical characterization of MIM capacitors with anodic titania. In this paper, we present fabrication and characterization of barrier-type anodic TiO_2 MIM capacitors with a high capacitance density of 33 fF/μm^2 and low leakage current density of 9.61×10^{-8} A/cm^2 at 1 V.

2. Fabrication process

Barrier-type anodic titania with rutile and anatase crystalline phases has been obtained by many authors

* Corresponding author. Tel.: +91 0416 2202360; fax: +91 0416 2243092.
E-mail address: psmallick@vit.ac.in (P.S. Mallick).

1369-8001/$ - see front matter © 2012 Elsevier Ltd. All rights reserved.
http://dx.doi.org/10.1016/j.mssp.2012.10.013

using various aqueous electrolytes, such as ammonium pentaborate (bor-H_2O) and sodium tetraborate [16,17]. Anodization of Ti using ammonium pentaborate in ethylene glycol (bor-gly) electrolyte has been demonstrated by a few authors [18,19]. However, many authors have worked on anodization of Al with bor-gly electrolyte, which results in crystalline barrier oxide with low defects [11,20]. It has been observed that bor-gly solution results in low leakage and high effective barrier height compared to bor-H_2O [20]. This indicates that bor-gly electrolyte is a promising candidate for preparation of barrier-type titania. In this paper, we demonstrate the anodization of Ti using ammonium pentaborate dissolved in ethylene glycol to form MIM capacitors.

The Al/TiO_2/Al structure was fabricated in the following manner. A bilayer of Ti/Al (15 nm/100 nm) was deposited using an electron-beam evaporator with a W filament at a pressure of 8×10^{-5} mbar over a 100-nm thermally oxidized SiO_2 on Si substrate. Here, Al acted as the bottom electrode, which controlled the thickness of TiO_2 during anodization. Ti film was potentiostatically anodized in a nonaqueous solution of ammonium pentaborate dissolved in ethylene glycol (20 g/l) by the same size of Pt cathode. Electrolyte solution was prepared by adding 17 g ammonium pentaborate for every 100 ml ethylene glycol [11]. Anodization was done for anodization voltages of 10 V, 15 V, and 20 V until the current density reduced to 1 $\mu A/cm^2$. To avoid etching of the bottom electrode, only three-quarters of the sample area was dipped in the electrolyte. Once cleaned thoroughly by deionized water, a 50-nm thick Al top electrode was deposited on the anodized samples using a thermal evaporator with a shadow mask area of $\sim$0.61 mm^2. Fig. 1 shows the scanning electron microscopy (SEM) cross-section of all three samples before top electrode deposition.

At higher anodization voltages (15 V and 20 V), the bottom Al electrode was also anodized. This formed a thin amorphous layer of $\sim$2 nm AlTiO (an alloy of both TiO_2 and Al_2O_3), which stopped further migration of oxygen ions into the Al electrode. Fig. 2 shows the depth profile of the three samples using secondary ion mass spectrometry (SIMS) in positive mode with 1 kVCs. This shows ion distribution of Ti, Al, O, Si, Ti-O, and Al-O. It was observed that the count of Al-O and Al was significantly near the TiO_2/Al interface that formed the AlTiO composite layer in T2 and T3 samples (Figs. 2b and 2c). However, in the T1 sample it was not significant due to the lower anodization voltage (10 V). The formation of AlTiO composite layer was due to outward migration of Al ions. However, Al ions rapidly decrease into the TiO_2 region because they migrate slower than Ti ions [16]. This composite layer reduced the effective thickness of the TiO_2 region. Fig. 3 shows the X-ray diffraction (XRD) spectra of samples prepared at various anodization voltages. The spectra showed that the prepared TiO_2 at lower anodization voltage had crystalline phases that were predominantly rutile with anatase and partially amorphous (Fig. 3a). At higher anodization voltages, the amorphous state was transferred to a crystalline/quasicrystalline state (anatase). The outer layer of the anodic film had an amorphous structure ($\sim$30%), which was stabilized by electrolyte-derived species, and a crystalline layer was available near the bottom electrode [16].

Crystallization of anodic titania has been studied by many authors. Some have reported that amorphous to crystalline transition occurs at low voltages (<10 V) [16,17,21]. Habazaki et al. have observed that during anodization the amorphous phase is transformed to anatase [16]. According to Vasil'eva et al., borate and fluoride electrolytes generally result in titania with rutile and anatase modifications respectively [17]. Felshe et al. have reported that anodic titania shows rutile phases at low anodization voltages [21]. Unfortunately, inconsistencies have been found in the experimental conditions for TiO_2 crystallization such as electrolyte temperature, electrolyte composition, and applied anodization voltage [16–21].

The crystallization process of our anodic TiO_2 has been addressed based on the observations of Habazaki et al.

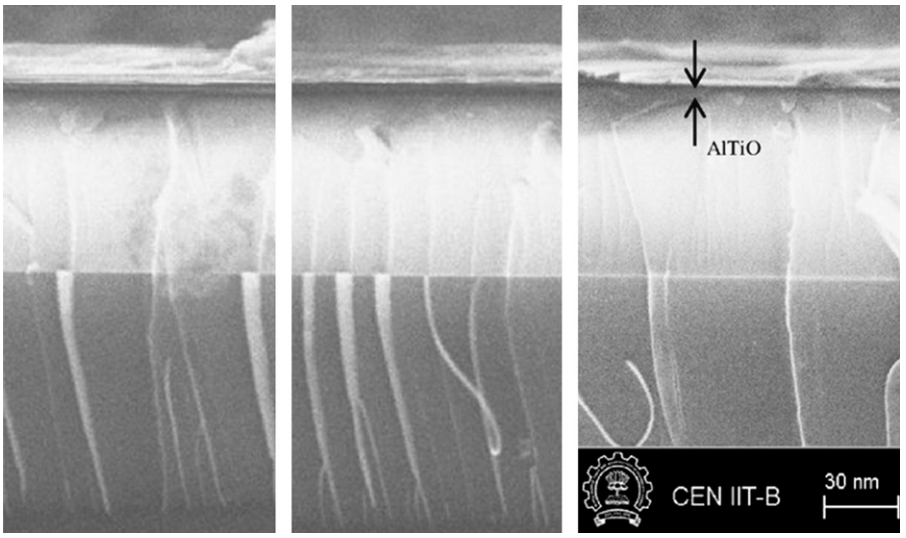

Fig. 1. SEM cross-section image of anodized region before top electrode deposition. Anodization voltage: (a) 10 V, (b) 15 V, (c) 20 V.

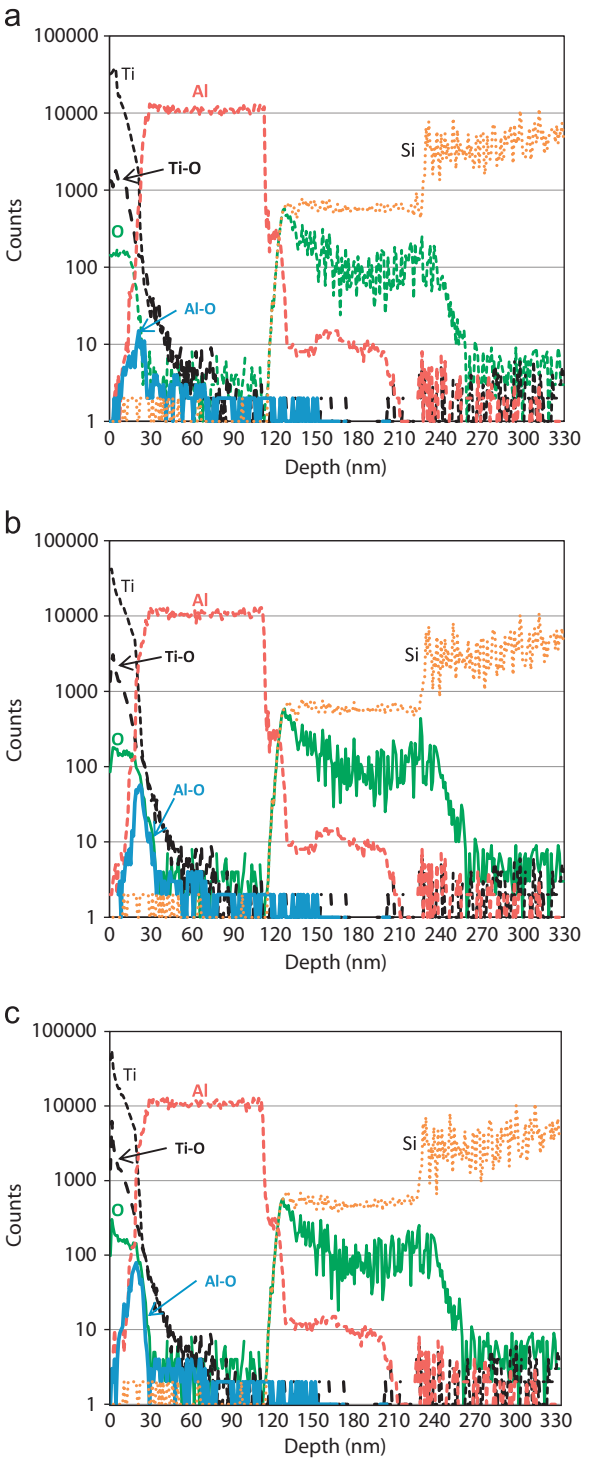

Fig. 2. SIMS depth profile of all three samples. Anodization voltage: (a) 10 V, (b) 15 V, (c) 20 V.

and Kar [16,22]. The applied anodization field affects the near insulator/metal interface with high energy. This forms a thin layer of rutile titania with bulk defect/bubbles (~1 nm) by inward migration of O^{2-} ions [16,22]. An amorphous titania layer has been formed over the rutile layer by outward migration of B ions [16]. After the formation of rutile, the inward migration of O^{2-} ions is suppressed by the high field crystalline (high ionic resistivity) and anodized alumina regions. In this case, amorphous to anatase phase transition occurs at defect sites above the rutile region at higher anodization voltages. The lower activation energy of bulk defects aids the heterogeneous nucleation of anatase titania [22]. Fig. 4 shows the crystallization processes during anodization.

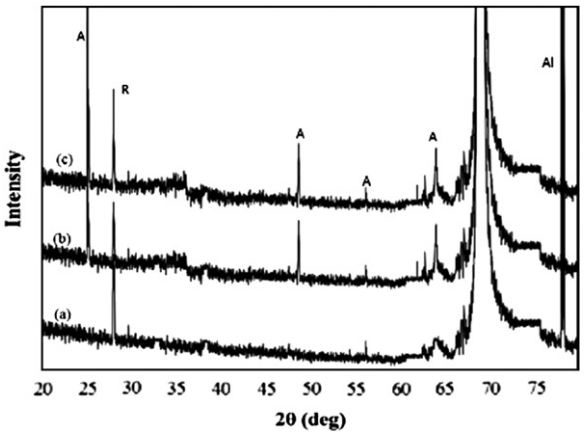

Fig. 3. XRD spectra of anodized samples at various anodization voltages: (a) 10 V, (b) 15 V, (c) 20 V (A: Anatase, R: Rutile).

3. Measurement results and discussion

3.1. C–V characteristics

The capacitance and leakage current were measured using an HP4155C semiconductor parameter analyzer. Fig. 5 shows measured *C–V* characteristics of MIM capacitors for 10 kHz at room temperature. The capacitance increased by about 2 fF/μm^2 for higher anodization voltage, which was due to improved crystalline properties. The thin AlTiO layer acted as interfacial layer between TiO_2 and the Al bottom electrode. This helps in the formation of capacitance and reduction of leakage current [23]. The linear (β) and quadratic (α) coefficients of capacitance are extracted using $C(V) = C_0(\alpha V^2+\beta V+1)$, where C_0 is the capacitance at bias voltage of zero. Extracted α (ppm/V^2) and β (ppm/V) for various anodization voltages are shown in the inset of Fig. 5. Value of α reduced from 1431 ppm/V^2 to 938 ppm/V^2 as anodization voltage increased from 10 V to 20 V. High capacitance density and low VCC at high anodization voltage ensured the reduction of traps/defects at the bulk and metal/dielectric interface. The obtained α values were comparable to those in earlier reports [2–5,11–13]. Recently it has been observed that VCC is inversely proportional to the square of the oxide thickness of the MIM capacitor [24]. Therefore, one can reduce VCC and leakage current density as per recommendations of ITRS by increasing the thickness of anodic TiO_2.

3.2. Frequency dependence of capacitance

Fig. 6 shows the measured frequency-dependent capacitance for various anodization voltages at 25 °C.

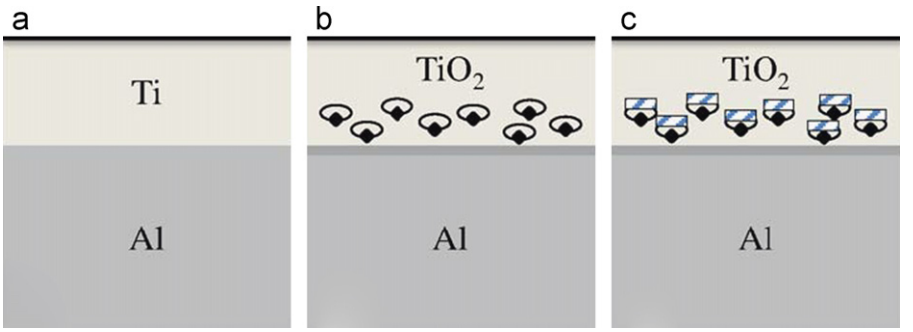

Fig. 4. Schematic view of processes during anodization: (a) initial growth of amorphous titania, (b) formation/nucleation of rutile (cube) with bulk defects (ellipse), (c) nucleation of amorphous to anatase (rectangle) at defect sites.

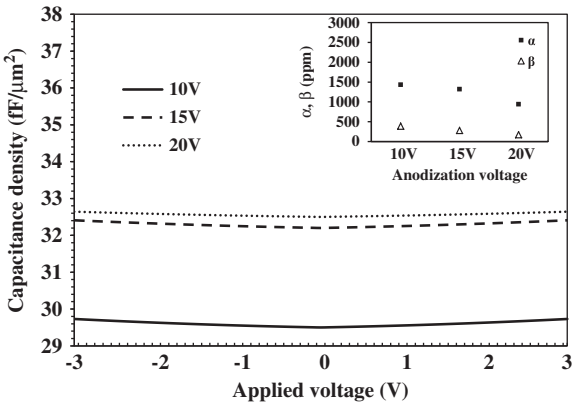

Fig. 5. C–V characteristics of anodic TiO_2 MIM capacitor at a temperature of 25 °C.

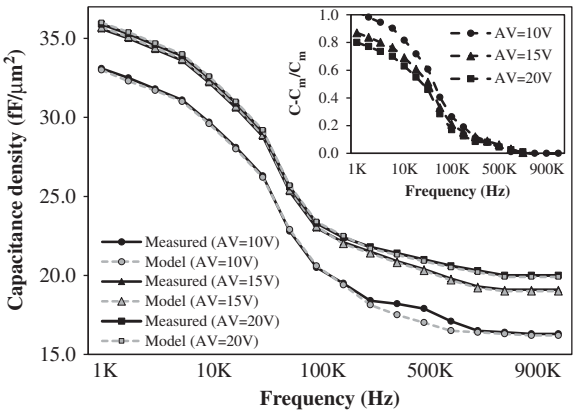

Fig. 6. Measured frequency dependent capacitance of anodic TiO_2 MIM capacitors for various anodization voltages.

We found that the capacitance was less sensitive to frequency and improved after 100 kHz at higher anodization voltages, which indicated formation of stronger dipolar polarization. We used Beaumont and Jacobs' electrode polarization model to explain the dispersion of capacitance with frequency, which was developed by hopping of carriers and field-dependent mobility.

In MIM capacitors, the mobile charges form a double layer near the electrodes when an AC signal is applied. The double layers are considered as free electrons, injected from electrodes or intrinsic oxygen vacancies [14]. By applying a voltage, the mobile charges are accumulated over a distance L_d from the electrode, called the Debye length. This modulation of accumulation region under an AC field is referred as 'electrode polarization'. According to the modified Beaumont and Jacobs model [14], the capacitance is

$$C = C_m\left(1+\frac{A}{\omega^{2n}\tau^{2n}}\right) \tag{1}$$

where C_m is the capacitance for no electrode polarization, expressed as $C_m=\varepsilon_0\,\varepsilon_r S/L$, with top electrode area S and oxide thickness L. In Eq. (1), the slowly varying quadratic second term has $(\omega\tau)^{2n}$ and is called the Jonscher response, with $0<n<1$. ω and τ are the angular frequencies of the AC signal and relaxation time of the oxide, respectively. Parameters A and τ are expressed as

$$A = \frac{2}{(2+\rho)^2}\frac{L}{L_D}, \tag{2}$$

$$\tau = \tau_0\frac{1}{(2+\rho)}\frac{L}{L_D}, \tag{3}$$

In eqs. (2) and (3), intrinsic relaxation time $\tau_0=\varepsilon_0\varepsilon_r/\sigma$ and Debye length $L_D=(\varepsilon_0\varepsilon_r k_B T/N_t q^2)^{1/2}$, where N_t is density of intrinsic defects and σ is conductivity of the dielectric. ρ is called the 'blocking parameter', which is a measure of the electrode transparency. $\rho=\alpha\nu(L/D)exp(-E_i/k_BT)$ where α and ν are hopping distance and hopping frequency normal to the interface, respectively, and D is bulk diffusion coefficient. For strongly injecting contacts, such as ohmic contacts, ρ tends to infinity, which yields $A=0$ and $C\approx C_m$. This indicates that space charge is not formed at the metal–dielectric interface. In contrast, when the contact is not injecting any charges, A is very large and ρ is very small. This describes how important the effect of space charge is [14]. We obtained the parameters of modified Beaumont and Jacobs model [14] by using measured capacitance C and considering $\alpha=0.5$ nm, $\nu=10^{12}$ Hz, $L=15$ nm, and interfacial energy barrier $E_i\approx 0.94$ eV for Al/TiO_2. For this model, with $L_D\approx 0.9$ nm, values of τ, N_t, and n were obtained for the best fit as anodization voltage was varied. These values are presented

in Table 1. Increasing anodization voltage decreased both defect density N_t and factor n. Hence, sensitivity of the TiO_2 MIM capacitor to frequency reduced. Compatibility of the model and measured results are illustrated in Fig. 6.

According to Kosjuk et al. [25], the second term of the model in Eq. 1 refers to the contribution of relaxation polarization in formation of capacitance, which is extracted using $(C - C_m)/C_m$ (Fig. 6 inset). This slowly varying term decreases in the order from 0.2 to 0.1. This reveals that the relaxation polarization is dominant at lower anodization voltages due to presence of large defects and slow relaxation time. At higher anodization voltages, the ionic polarization improves as the amorphous state transfers to crystalline with low defect density.

3.3. I–V characteristics

The leakage characteristics were measured by injecting electrons from the Al bottom layer to the TiO_2 layer (forward bias) and from the top Al layer to the TiO_2 layer (reverse bias). Fig. 7 shows the measured leakage current density of all the samples at room temperature for different applied voltages, and Fig. 8 shows the measured leakage current density of sample T3 at various temperatures for different applied voltages. The *I–V* characteristics obtained is asymmetric. This was due to nonuniform crystalline structure and anodization of Al (AlTiO), which resulted in different effective barrier heights at the top Al/TiO_2 and bottom TiO_2/Al interfaces. Also, it is clear that leakage current was more sensitive to temperature in forward than reverse bias. To explain these properties of anodic TiO_2, conduction mechanisms such as Schottky emission (SE) and Poole–Frenkel (PF) emission were studied.

In Fig. 7, the higher slope until 0.3 V indicates the SE tunneling of electrons to the unoccupied defect or trap states near the metal insulator interface. Moderate fields, between 0.3 V and 1 V, were dominated by the PF tunneling emission mechanism, where the trapped electrons enhanced from defect states to conduction states of the dielectric. Above 1 V, PF saturation was observed. This was due to the trap barrier height being reduced to zero at higher fields, thus the charged (coulombic) traps have no effect on the carriers [26]. According to [27], the expression for leakage current density due to SE and PF mechanisms is,

$$J_{SE} = AT^2 \exp\left\{-\frac{1}{kT}\left(q\varphi_B - \beta_{SE}\sqrt{E}\right)\right\} \quad (4)$$

$$J_{PF} = CE\exp\left\{-\frac{1}{\xi kT}\left(q\varphi_{PF} - \beta_{PF}\sqrt{E}\right)\right\} \quad (5)$$

where A is Richardson's constant ($1200/cm^2/k^2$) and C is the proportionality constant. Φ_B and Φ_{PF} are Schottky barrier and trap barrier heights, respectively, and E is applied electric field. The constants β_{SE} and β_{PF} are expressed as $\beta_{SE} = (q^3/4\pi\varepsilon_0\varepsilon_r)^{1/2}$ and $\beta_{PF} = (q^3/\pi\varepsilon_0\varepsilon_r)^{1/2}$ where ε_0 is permittivity of the free space and ε_r is dielectric constant of the insulator. The dielectric constant ε_r can vary from 40 to 120 depending on crystalline property and structural defects. We considered it as 60 due to the presence of an amorphous layer and rapid degradation of capacitance with frequency. Barrier height

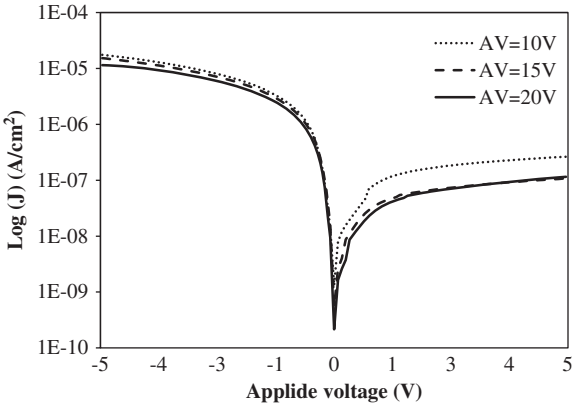

Fig. 7. Measured leakage current density for all samples at room temperature.

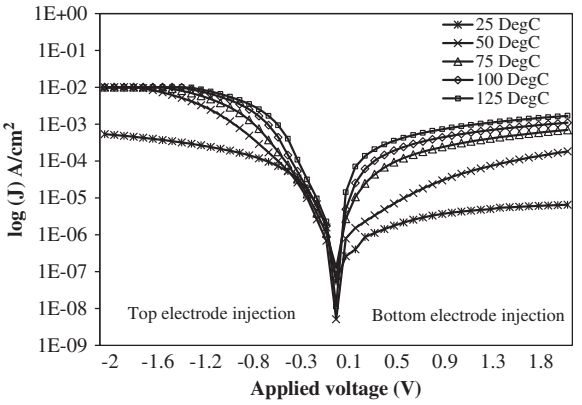

Fig. 8. Measured leakage current density at various temperatures for T3 sample.

Table 1
Measured and extracted parameters of anodic TiO_2 at various anodization voltages.

Anodization voltage, sample name, and effective thickness of TiO_2	Measured capacitance density at 1 V and 10 kHz (fF/μm²)	Measured conductance at 1 V and 1 MHz ($\times 10^{-12}$ S/cm)	Extracted model parameters				
			ρ	τ (s)	A	N_t (cm^{-3})	n
10 (T1), ~17 nm	29.6	2.2	4.4 ± 2	3.72×10^{-5}	0.79 ± 0.2	6.6×10^{18}	0.2 ± 0.1
15 (T2), ~15 nm	32.2	0.97	6.1 ± 2	1.17×10^{-5}	0.57 ± 0.2	7.2×10^{17}	0.1 ± 0.1
20 (T3), ~14 nm	32.5	0.90	8.6 ± 2	1.01×10^{-5}	0.32 ± 0.2	3.1×10^{17}	0.1 ± 0.1

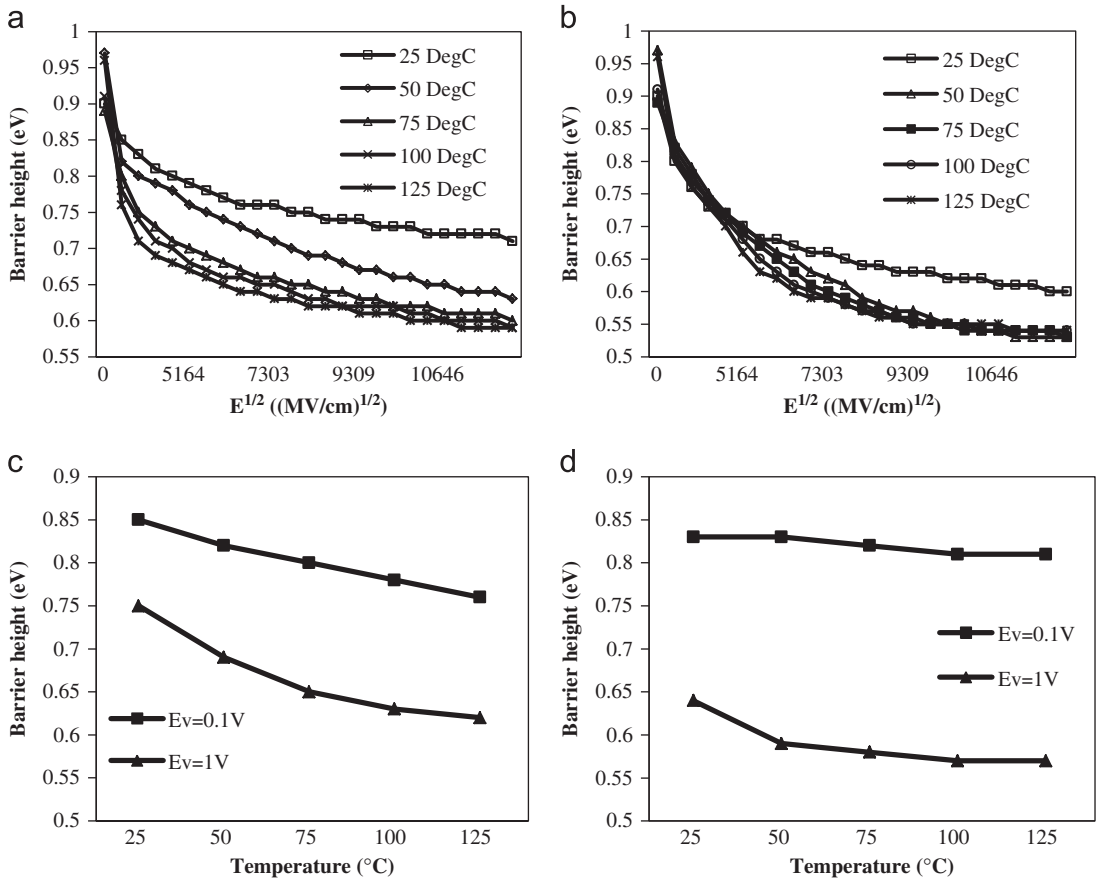

Fig. 9. Extracted barrier height for T3 sample at various temperatures. (a) Forward bias, (b) Reverse bias, (c) Forward bias at $E^{V=0.1V}$, $E^{V=1V}$, (d) reverse bias at $E^{V=0.1V}$, $E^{V=1V}$.

was extracted as a function of applied electric field E for various temperatures using Eq. 4. Figs. 9a and b shows the extracted barrier height for T3 sample (anodized at 20 V) at forward and reverse bias, respectively. As expected, a small difference of 0.05 eV in barrier height at the bottom Al/TiO_2 and top Al/TiO_2 interfaces was observed for the low fields. This confirms the formation of AlTiO at the bottom electrode interface, which considerably reduced the overall leakage. Figs. 9c and 9d shows that the extracted barrier heights for various temperatures at two different fields corresponded to applied voltages of 0.1 V and 1 V. Compared to reverse bias, a large change in barrier height was observed for increase in temperature at forward bias (bottom injection). This shows that the crystalline TiO_2 region and interface were sensitive to temperature. A similar observation has recently been reported for atomic layer deposition of TiO_2 in MIM capacitors [28].

Barrier height reduction with temperature increment can be explained by the observations of Hickmott in anodized Al_2O_3 thin films [29]. It has been concluded that the effective tunneling barrier of the empty traps decreases with increase in temperature [29]. To study further, the PF tunneling mechanism was used to extract the trap barrier heights at various temperatures for forward and reverse bias. From the temperature-dependent leakage characteristics shown in Fig. 8, a $ln\ (J/E)$ versus $1/T$ plot was extracted for forward bias (Fig. 10a). Using this plot, trap barrier height was extracted for specified fields at different temperatures (Fig. 10b). By extrapolating the obtained curves to a zero field, the intrinsic trap barrier height can be obtained [30]. A similar procedure was followed to extract trap barrier height in reverse bias (Figs. 10c and 10d). It is clear that traps available near the bottom electrode (in crystalline region) were more sensitive to temperature, whereas traps in the amorphous region were stable. Fig. 10b shows that intrinsic trap barrier height ($E^{1/2}=0$) of the crystalline region (near bottom electrode) was largely degraded with increase in temperature. At reverse bias, the amorphous region showed a trap barrier height of $\sim$0.15 eV, which was stable with temperature.

The partial crystalline structure of anodic TiO_2 and interfacial layer cause asymmetric leakage/breakdown at positive and negative half cycles. In a big wafer level anodization, there is a possibility of nonuniform oxide thickness due to unequal cathode size with wafer and/or nonuniform anodic field distribution. This may lead to undesirable effects in circuit level, however, it is purely a statistical impact. Process variations can be studied in detail with respect to anodization voltage, electrolyte composition, and temperature.

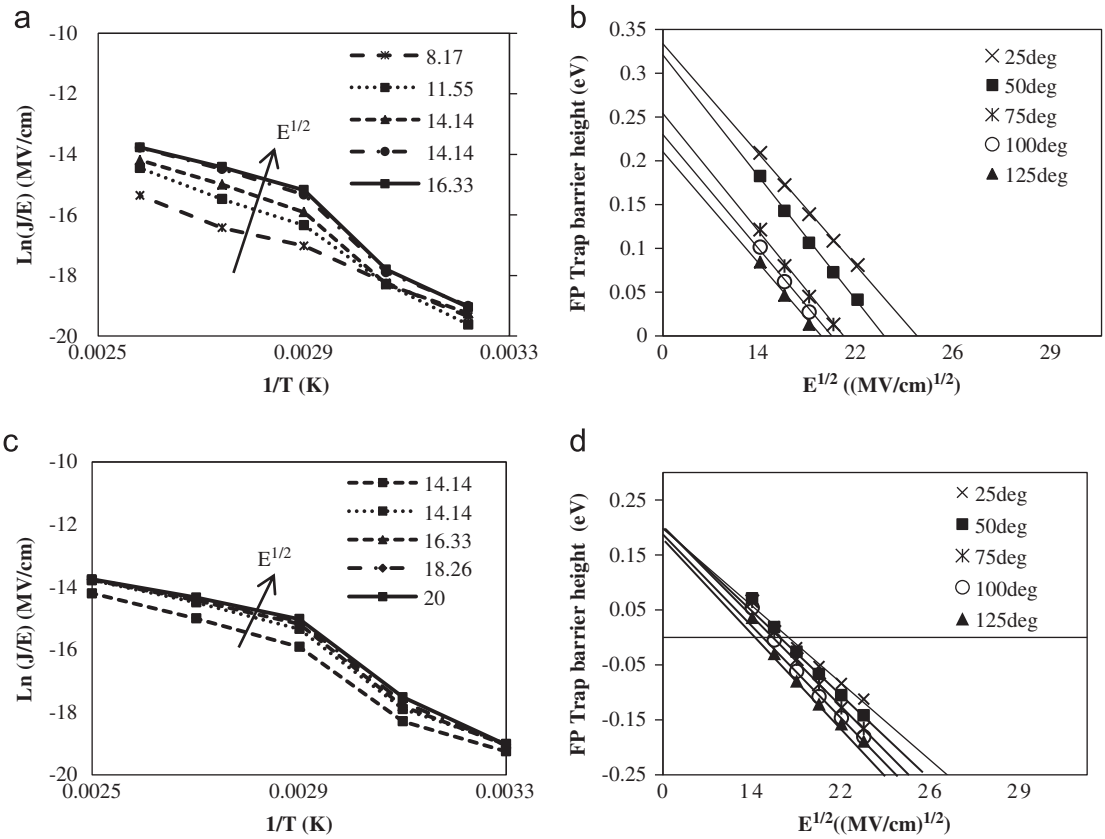

Fig. 10. Extraction of PF trap barrier heights for forward and reverse bias: (a) Ln (J/E) versus 1/T plot for Forward bias, (b) PF trap barrier height for forward bias at various temperatures, (c) Ln (J/E) versus 1/T plot for reverse bias, (d) PF trap barrier height for reverse bias at various temperatures.

4. Conclusion

The fabricated capacitor using anodic oxidation shows a high capacitance density of 33 fF/μm^2 and leakage current density of 9.61×10^{-8} A/cm^2 at 1 V. It is observed that crystalline and polarization processes are improved at higher anodization voltages, which reduce the VCC and sensitivity of the capacitance with frequency. The asymmetric leakage characteristics in forward and reverse bias were studied using SE and PF emission mechanisms. It was observed that the trap barrier height at the top electrode interface was deeper than at the bottom electrode interface. Anodic oxidation of barrier-type TiO_2 allows effective low-cost fabrication of high-density MIM capacitors for future RFICs and MMICs.

Acknowledgments

We would like to acknowledge financial support by Indian Nanoelectronics User's Program (INUP), Government of India, through IIT-Bombay. We would also like to thank Prof. A. Q. Contractor, Dr. K. Nageswari, Mr. Ramkumar, and Mr. Yaksh, IIT-Bombay for their support, as well as Sophisticated Analytical Instrument Facility (SAIF), IIT-Bombay, for providing the SIMS facility.

References

[1] International Technology Roadmap for Semiconductor (ITRS) 2010, Report on RF and Analog/Mixed Signal design.
[2] F. Mondon, S. Blonkowski, Electrical characterisation and reliability of HfO_2 and Al_2O_3–HfO_2 MIM capacitors, Microelectronics Reliability 43 (2003) 1259–1266.
[3] S.-Y. Lee, H. Kim, P.C. McIntyre, Atomic layer deposition of ZrO_2 on W for metal- insulator-metal capacitor application, Appl. Phys. Lett. 82 (2003) 2874–2876.
[4] S. Becu, S. Cremer, J.L. Autran, Capacitance non-linearity study in Al_2O_3 MIM capacitors using an ionic polarization model, Microelectronic Engineering 83 (2006) 2422–2426.
[5] C.H. Cheng, S.H. Lin, K.Y. Jhou, W.J. Chen, C.P. Chou, F.S. Yeh, J. Hu, M. Hwang, T. Arikado, S.P. McAlister, A. Chin, High Density and Low Leakage Current in TiO_2 MIM Capacitors Processed at 300°C, IEEE Electron Device Letters 29 (2008) 845–847.
[6] A. Wisitsoraat, A. Tuantranont, E. Comini, G. Sberveglieri, W. Wlodarski, Characterization of n-type and p-type semiconductor gas sensors based on NiO_x doped TiO_2 thin films, Thin Solid Films 517 (2009) 2775–2780.
[7] M. Gratzel, Sol-gel processed TiO_2 films for photovoltaic applications, Journal of Sol-Gel Science and Technology 22 (2001) 7–13.
[8] K. Chiang, C. Lai, A. Chin, H. Kao, S. McAlister, and C. Chi, Very high density RF MIM capacitor compatible with VLSI, in Proc. IEEE MTT-S Dig. (2005) 287–290.
[9] A.G. Mantzila, M.I. Prodromidis, Performance of impedimetric biosensors based on anodically formed Ti/TiO_2 electrodes, Electroanalysis 17 (2005) 1878–1885.
[10] M. Stamate, G. Lazar, I. Lazar, Dimensional effects observed for the electrical, dielectrical and optical properties of TiO_2 DC magnetron thin films, J Mater Sci: Mater Electron 20 (2009) 117–122.
[11] D. Kannadassan, R. Karthik, M.S. Bhagini, P.S. Mallick, Nanostructured barrier type anodic oxide metal–insulator–metal capacitors, J. Nanoelect 7 (2012) 400–404Optoelect 7 (2012) 400–404.

[12] E. Hourdakis, A.G. Nassiopoulou, High performance MIM capacitor using anodic alumina dielectric 90 (2012) 12Microelectron. Eng. 90 (2012) 12–14.
[13] E. Hourdakis, A.G. Nassiopoulou, MIM High-density, capacitors with porous anodic alumina dielectric 57 (2010) 2679–2683IEEE Transactions on Electron Devices 57 (2010) 2679–2683.
[14] P. Gonon, C. Valláe, Modeling of nonlinearities in the capacitance-voltage characteristics of high- k metal-insulator-metal capacitors, Appl. Phys. Lett. 90 (2007) 142906.
[15] J.W. Diggle, T.C. Downie, C.W. Goulding, Anodic oxide films on aluminum, Chem. Rev 69 (1969) 365–405.
[16] H. Habazaki, M. Uozumi, H. Konno, K. Shimizu, P. Skeldon, G.E. Thompson, Crystallization of anodic titania on titanium and its alloys, Corrosion Science 45 (2003) 2063–2073.
[17] M.S. Vasil'eva, V.S. Rudnev, L.M. Tyrina, I.V. Lukiyanchuk, N.B. Kondrikov, P.S. Gordienko, Phase composition of coatings formed on titanium in borate electrolyte by microarch oxidation, Russian Journal of Applied Chemistry 75 (2002) 569–572.
[18] G.H. Gleaves, R.A. Collins, G. Dearnaley, A further investigation of the influence of implanted foreign ion species on the anodic oxidation of Ti, J Electrochemical Society 137 (1982) 51–65.
[19] R.J. Soukup, Observations of negative resistance in Ti/TiO_2/Au diodes, J. Appl. Phys. 43 (1972) 3431–3435.
[20] T.W. Hickmott, Electrolyte effects on charge, polarization, and conduction in thin anodic Al_2O_3 films II. Temperature dependent conduction and a Meyer- Neldel relation, J Appl. Phy 102 (2007) 1–11.
[21] A. Felske, W.J. Plieth, Raman spectroscopy of titanium dioxide layers, Electrochimica Acta 34 (1989) 75–77.
[22] P. Kar, Effect of anodization voltage on the formation of phase pure anatase nanotubes with doped carbon, Inorganic Materials 46 (2010) 377–382.
[23] T.H. Phung, P. Steinmann, R. Wise, Y-C. Yeo, C. Zhu, Modeling the negative quadratic VCC of SiO_2 in MIM capacitor, Elect. Dev. Lett 32 (2011) 1671–1673.
[24] J-C. Woo, Y-S. Chun, Y-H. Joo, C-I. Kim, Low leakage current in metal-insulator-metal capacitors of structural $Al_2O_3/TiO_2/Al_2O_3$ dielectrics, Appl. Phys, Lett 100 (2012) 1–3.
[25] L.M. Kosjuk, L.L. Odynets, Polarization processes in anodic oxide films, Thin Solid Films 302 (1997) 235–238.
[26] G. Southwick, J. Reed, C. Buu, R. Butler, G. Bersuker, W.B. Knowlton, Limitations of Poole–Frenkel conduction in bilayer HfO_2/SiO_2 MOS devices, IEEE Trans. Device and Materials Reliability 10 (2010) 201–207.
[27] S. Chakraborty, M.K. Bera, S. Bhattacharya, C.K. Maiti, Current conduction mechanism in TiO_2 gate dielectrics, Microelectronic Engineering 81 (2005) 188–193.
[28] M. Seo, S.H. Rha, S.K. Kim, J.H. Han, W. Lee, S. Han, C.S. Hwang, The mechanism for the suppression of leakage current in high dielectric TiO_2 thin films by adopting ultra-thin HfO_2 films for memory application, Journal of Applied Physics 110 (2011) 024105–024111.
[29] T.W. Hickmott, Temperature-dependent Fowler–Nordheim tunnelling and a compensation effect in anodized Al-Al_2O_3-Au diodes, J. Appl. Phys 97 (2005) 104505–104513.
[30] C.-C. Yeha, T.P. Ma, Frenkel–Poole trap energy extraction of atomic layer deposited Al_2O_3 and Hf_xAl_yO thin films, Applied Physics Letters 91 (2007) 113521–113523.